

See discussions, stats, and author profiles for this publication at: <https://www.researchgate.net/publication/326561828>

Flight Dynamics Modeling and Control of a Novel Catapult Launched Tandem-Wing Micro Aerial Vehicle With Variable Sweep

Article in IEEE Access · July 2018

DOI: 10.1109/ACCESS.2018.2858293

CITATIONS

11

READS

1,537

5 authors, including:



Liang Gao

Harbin Institute of Technology

11 PUBLICATIONS 37 CITATIONS

[SEE PROFILE](#)



Hongzhe Jin

Harbin Institute of Technology

56 PUBLICATIONS 599 CITATIONS

[SEE PROFILE](#)



Jie Zhao

Harbin Institute of Technology

408 PUBLICATIONS 3,069 CITATIONS

[SEE PROFILE](#)



Yanhe Zhu

Harbin Institute of Technology

209 PUBLICATIONS 1,733 CITATIONS

[SEE PROFILE](#)

Some of the authors of this publication are also working on these related projects:



Pneumatic Artificial Muscle [View project](#)



Design, control and operation of the variable stiffness manipulator [View project](#)

Received June 2, 2018, accepted July 15, 2018, date of publication July 23, 2018, date of current version August 20, 2018.

Digital Object Identifier 10.1109/ACCESS.2018.2858293

Flight Dynamics Modeling and Control of a Novel Catapult Launched Tandem-Wing Micro Aerial Vehicle With Variable Sweep

LIANG GAO^{ID}, HONGZHE JIN^{ID}, JIE ZHAO, HEGAO CAI, AND YANHE ZHU

State Key Laboratory of Robotics and System, Harbin Institute of Technology, Harbin 150001, China

Corresponding author: Yanhe Zhu (yhzhu@hit.edu.cn)

This work was supported in part by the Joint Research Fund between the National Natural Science Foundation of China and Shenzhen under Grant U1713201 and in part by the National Natural Science Foundation of China under Grant 61004076.

ABSTRACT In this paper, the variable sweep is used as a replacement for the conventional control surfaces for flight control on a tandem-wing micro aerial vehicle (MAV). This configuration allows the MAV to be folded into and launched from a tubular catapult while also retaining an adequately high effectiveness and a simple structure. As new control inputs, the four sweep angles of the MAV are planned as symmetric and asymmetric morphing to eliminate the reactive forces between the airfoils and fuselage during morphing. The aerodynamic characteristics of the MAV are presented through numerical simulations to study the effects of variable sweep morphing. An accurate nonlinear multibody dynamic model of the variable sweep MAV is established using the Kane method. Next, open-loop dynamic responses of sweep morphing based on the nonlinear dynamic model are analyzed and compared with the responses caused by the elevons control mode to examine the control effectiveness. Moreover, a flight control law based on sweep control is designed and verified using a height and yaw tracking simulation with different actuator response rates. The results show that the sweep control mode produces weaker coupling between the longitudinal and lateral dynamics than the elevons control mode and that the innovative approach for flight control is feasible and effective.

INDEX TERMS Tandem-wing, variable sweep, catapult launch, dynamic coupling, morphing aircraft, Kane method.

I. INTRODUCTION

Unmanned aerial vehicle (UAV) systems have been broadly applied in military and civilian fields, such as in monitoring and mapping [1], across the globe in recent years, and the performance requirements are becoming increasingly stringent. Among the various forms of UAVs, there are certain types of MAVs that have a wingspan scale of less than 1 m [2] with folded airfoils that can be launched from a tubular catapult and have the airfoils deployed while in free flight [3]. The folding technology can reduce the space required for an MAV and allow easy storage and transportation, and the short fuselage structure without an undercarriage can considerably reduce the vehicle weight [4]. Moreover, the catapult approach has higher security, less wind influence, faster take-off speed and better launch stability than the other launching modes, and it does not require a runway, thereby allowing MAVs to be launched from other aircraft or underwater [5], [6].

The use of morphing wings, including inflatable wing [7], composite bendable-wing [8], and flexible membrane wing [9], for MAVs to fit into a small container has been extensively studied by many researchers. There is also a means of structural deformation such that MAVs deploy folded airfoils by rotating the airfoils from the initial positions (at which they were attached and aligned parallel to the fuselage) to positions perpendicular to the fuselage [6], [10], [11]. Although morphing wings and structural deformation can meet the folding requirement, space limitations will result in a considerable decrease in the effectiveness of the control surfaces because of the small areas, moment arms and available dynamic pressures as well as the more complex structural arrangements [9].

In these situations, additional equipment or an innovative approaches can be used to assist or even replace the conventional control surfaces to enhance flight performance. A cycle variable pitch propeller system [12] and alterable thrust

direction [13] inspired by thrust vectoring techniques were developed to improve the maneuverability and agility of UAVs. Many research institutions have investigated biologically inspired gull-wing aircraft using symmetric or asymmetric morphing to generate pitch or roll moment for flight control [14]–[16]. Other approaches, such as telescope wing morphing [17] and the combination of variable sweep and variable span [18], have dramatically improved the maneuverability of UAVs. However, flight control cannot be achieved solely using methods employing thrust vectoring techniques, and such methods will lead to a more complex MAV construction. The other approaches mentioned above cannot easily meet the aim of folding an MAV into a container.

Considering the aforementioned analysis, we propose a novel tandem-wing MAV with four variable wings that can be folded into a tube launcher and deployed in free flight after being launched by a catapult. The most distinctive feature of the proposed MAV is that it has four variable sweep wings employing various combinations of sweep angles for attitude control to replace the traditional control surfaces. Variable sweep technology can satisfy the aerodynamic requirements of both high and low speeds, thereby expanding the flight envelope. [19] There are an increasing number of applications of variable sweep on MAVs to enhance perching maneuvers [20], [21], achieve a high aerodynamic efficiency and greater ease of launching [22], or optimize the flight dynamics of each maneuver [23]. Most studies have focused on symmetric sweep morphing only for longitudinal flight control [24]; in contrast, only a few studies have investigated asymmetric sweep morphing for lateral flight control. Tong et al. explored the concept of asymmetric variable sweep wing on traditional aircraft for roll control as well as for pitch control [25]. However, this configuration will result in large changes in the aerodynamic and configuration parameters during the sweep variation and lead to three-axis dynamic response variations that must be trimmed using the control surfaces. Therefore, it is meaningful to explore a novel variable sweep concept on a tandem-wing MAV to entirely displace the traditional control surfaces.

Inspired by the above discussions, a tandem-wing MAV with four variable sweep airfoils using symmetric morphing for longitudinal maneuverability and asymmetric morphing for lateral maneuverability is a potentially practical approach to address the difficulty in mounting control surfaces on MAVs. Compared with the existing results, the main contributions of this paper lie in the following.

(1) The novel catapult launched tandem-wing MAV, which has no traditional control surfaces, uses symmetric morphing of the variable sweep airfoils for pitch control and asymmetric morphing for roll control, thereby decreasing the configuration complexity and maintaining control effectiveness.

(2) Coordinated allocation sweep angles of the canards and wings can weaken the coupling between longitudinal and lateral dynamics, and the shift in the neutral point can be



FIGURE 1. Catapult launch of the previous tandem-wing MAV prototype [26].

controlled within a small range by a configuration change compared with generic variable sweep aircraft.

To the best of the authors' knowledge, variable sweep technology has not been applied on tandem-wing aircraft. An MAV with four sweep angles as new control inputs is a complex, nonlinear, time-varying dynamic system, and therefore, systemic work including aerodynamic analysis, dynamics modeling, flight control and simulation is presented. In Section II, the effects of variable sweep on the aerodynamic characteristics are investigated using computational fluid dynamics (CFD) and the vortex lattice method (VLM), and multiple sweep inputs have been optimized to weaken the coupling between longitudinal and lateral dynamics. In Section III, the nonlinear multibody dynamic model of the variable sweep MAV is built using the Kane method. In Section IV, the open-loop dynamic responses of symmetric and asymmetric sweep morphing are numerically simulated and compared with the responses obtained using the elevons control mode to examine the control effectiveness of the variable sweep approach, and a flight control law is also designed to validate the feasibility and performance of the sweep control mode.

II. VARIABLE SWEEP MAV CONFIGURATION AND AERODYNAMIC ANALYSIS

A. CONFIGURATION OF THE MAV

Catapult launched flight experiments have been performed using the previous tandem-wing MAV prototype and demonstrated excellent performance, as shown in Fig. 1 [26]. On that basis, we modified the unfolding airfoil mechanism from a passive drive to an active drive; a schematic of the MAV is shown in Fig. 2. Four actuators are housed in the fuselage, driving the corresponding airfoils to unfold or change their sweep angle. The canards and wings of the MAV have the same size to improve the load capacity and allow it to easily maintain longitudinal balance. To reduce the effect of downwash caused by the canard, the wings are designed to be located above the canards. After catapult launching, the MAV is deployed, with the canards rotating forward by 90° and the wings rotating backward by 90° , driven by the corresponding

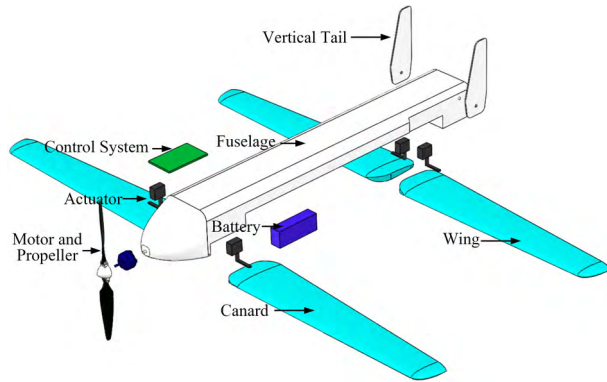


FIGURE 2. Exploded oblique view of the variable sweep MAV.

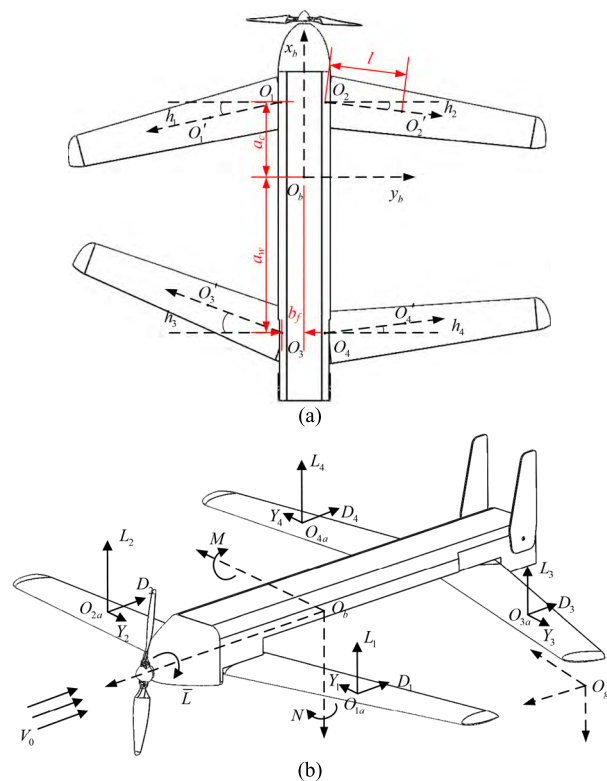


FIGURE 3. Aerodynamic force and moment on the variable sweep MAV. (a) Parameter definitions. (b) Aerodynamic characteristics.

actuator. To reduce the complexity of the airfoils' movement, the canards can sweep backward and the wings can sweep forward from 0° to 30° . The airfoils are made of light foam and carbon fiber materials to guarantee adequate strength and a fast response. The vertical tails are used to improve lateral stability.

O_b is the mass center of the fuselage, O_i is the center of rotation for each airfoil, O'_i is the mass center of each airfoil, the distance to O_i is l , O_{ia} is the aerodynamic center of each airfoil, h_i is the sweep angle of the airfoils, and $i = 1, 2, 3$, and 4 denote the left canard, right canard, left wing and right wing, respectively, as viewed from the tail of the aircraft

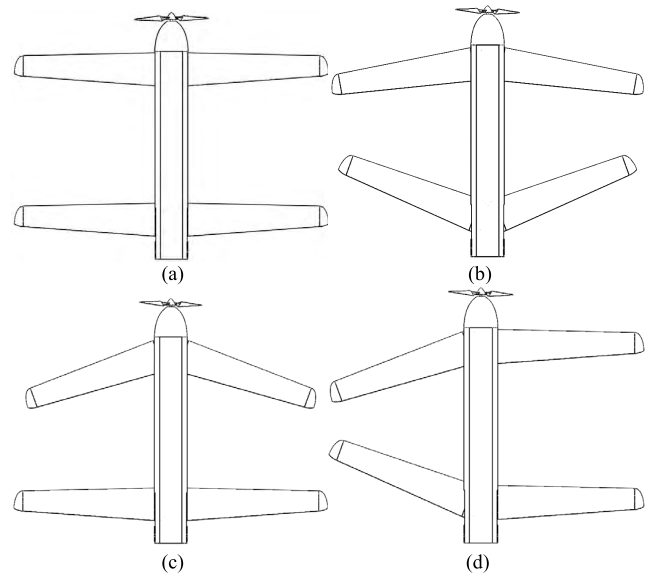


FIGURE 4. Several sweep configurations of the MAV. (a) No sweep. (b) Dash configuration. (c) Longitudinal maneuver. (d) Lateral maneuver.

TABLE 1. Main parameters of the aircraft.

Symbol	Unit	Value
Length l_f	m	0.72
b	m	0.89
c_A	m	0.077
m	kg	1.668
m_a	kg	0.08
J_x	$\text{kg}\cdot\text{m}^2$	7.9×10^{-4}
J_y	$\text{kg}\cdot\text{m}^2$	2.42×10^{-2}
J_z	$\text{kg}\cdot\text{m}^2$	2.43×10^{-2}
J_{xz}	$\text{kg}\cdot\text{m}^2$	1.14×10^{-3}
J_x^a	$\text{kg}\cdot\text{m}^2$	1.09×10^{-3}
J_y^a	$\text{kg}\cdot\text{m}^2$	2.6×10^{-5}
J_z^a	$\text{kg}\cdot\text{m}^2$	1.12×10^{-3}
l	m	0.14
a_c	m	0.165
a_w	m	0.235
b_f	m	0.04
c	m	0.015

shown in Fig. 3(a). In the initial state, the sweep angles are all equal to zero. A clockwise sweep angle rotating is positive from the top view; thus, h_2 and $h_3 \in [0^\circ, 30^\circ]$, h_1 and $h_4 \in [-30^\circ, 0^\circ]$. The main configuration parameters of the MAV are shown in Table 1. J_{yz}^f and J_{xy}^f are neglected because of the approximate symmetry about the fuselage coordinate plane Oxz , and the inertia tensors J_{xy}^a , J_{xz}^a and J_{yz}^a about the airfoil are also neglected because they are approximately zero.

B. AERODYNAMIC CHARACTERISTICS OF THE VARIABLE SWEEP MAV

The aerodynamic characteristics of each airfoil with variations in the sweep angles are shown in Fig. 3(b). Allocating the sweep angles rationally, the MAV has several configurations, namely, no sweep, dash configuration, longitudinal maneuver and lateral maneuver, as shown in Fig. 4. The initial

state is the no sweep configuration for loitering. Longitudinal maneuvers can be realized by symmetric morphing. When both of the canards sweep backward ($h_1 = -h_2, h_3 = h_4 = 0$), the shift in the aerodynamic center of the canards leads to a negative pitch moment relative to the center of mass, and the side forces Y_1 and Y_2 offset each other. Moreover, a positive pitch moment is generated when the wings sweep forward ($h_3 = -h_4$). Thus, by having the canards sweep backward and the wings sweep forward, one can trim the flight state without an elevator for the dash configuration and eliminate trim drag. Under the condition of asymmetric morphing ($h_2 = h_4 = 0, h_1 = -h_3$), the shift in the aerodynamic center of the left canard and the wing leads to a negative roll moment relative to the center of mass and an opposite roll moment under the condition of inverse morphing. However, the side forces Y_1 and Y_3 will lead to a positive yaw moment relative to the center of mass, and the drag is asymmetric ($D_2 + D_4 > D_1 + D_3$), leading to a yaw moment; the longitudinal balance is also broken with a shift in the aerodynamic center. Thus, notable coupling effects will be produced on the three axes and cannot be neglected.

The four variable sweep angles $[h_1, h_2, h_3, h_4]$ as control inputs are redundant and complex; thus, we allocated the four sweep angles and defined δ_e and δ_a as the control input for symmetric and asymmetric morphing to take on the roles of the conventional elevator and aileron, respectively. This mode is similar to the use of elevons on a flying wing. The two channels are separated and described by the following formulas for the mode that can also maximally eliminate the reactive force between the airfoils and fuselage during morphing:

$$\delta_e = \begin{cases} h_1 = -h_2, h_3 = h_4 = 0, & \delta_e < 0 \\ h_3 = -h_4, h_1 = h_2 = 0, & \delta_e > 0 \end{cases} \quad (1)$$

$$\delta_a = \begin{cases} h_1 = -h_3, h_2 = h_4 = 0, & \delta_a < 0 \\ h_2 = -h_4, h_1 = h_3 = 0, & \delta_a > 0 \end{cases} \quad (2)$$

In fact, the two canards and two wings in the symmetric condition or both sides in the asymmetric condition will sweep at the same time to ensure that the morphing MAV tracks the control command. However, the effects of dynamic motions hinder the accurate modeling of the MAV's aerodynamics; thus, we define the inputs as described above to greatly facilitate the aerodynamic modeling and follow-up research studies. The rudder is temporarily neglected in this study, and turning maneuvers are realized by the centripetal force formed by the horizontal lift component through asymmetric morphing to allow the aircraft to bank.

The morphing response is sufficiently fast such that the effects of unsteady aerodynamic force produced by morphing are negligible, and the aerodynamic forces and moments are achieved under the quasi-steady assumption. According to the input definition and quasi-steady assumption, the aerodynamic force and moment coefficients of the variable sweep MAV are relative to not only δ_e and δ_a but also to the attack

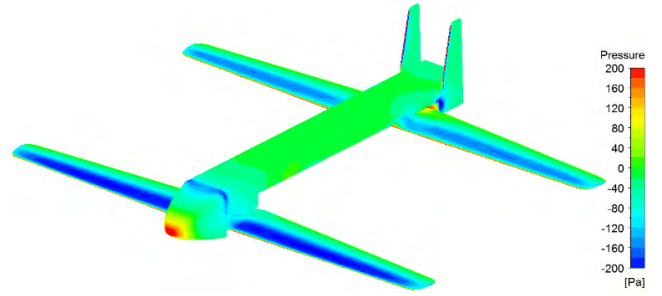


FIGURE 5. Pressure distribution on the tandem-wing MAV.

angle α and sideslip angle β , as expressed by the following equations:

$$\begin{cases} C_L = C_{L0} + C_{L\alpha}\alpha + C_{L\delta_e}\delta_e + C_{L\delta_a}\delta_a \\ C_D = C_{D0} + C_{D\alpha}\alpha + C_{D\delta_e}\delta_e + C_{D\delta_a}\delta_a \\ C_Y = C_{Y\beta}(\alpha)\beta + C_{Y\delta_a}\delta_a \\ C_l = C_{l\beta}(\alpha)\beta + C_{lp}p + C_{lr}r + C_{l\delta_a}\delta_a \\ C_m = C_{m0} + C_{m\alpha}\alpha + C_{m\beta}\beta + C_{mq}q + C_{m\delta_e}\delta_e \\ \quad + C_{m\delta_a}\delta_a \\ C_n = C_{n\beta}(\alpha)\beta + C_{np}p + C_{nr}r + C_{n\delta_a}\delta_a \end{cases} \quad (3)$$

where C_L , C_D , C_Y , C_l , C_m and C_n are the coefficients of lift, drag, side force, roll moment, pitch moment and yaw moment, respectively. The subscript “0” represents the zero-lift coefficient. C_{ij} is the aerodynamic derivative, where $C_{ij} = \partial C_i / \partial j$.

C. AERODYNAMIC ANALYSIS BY NUMERICAL SIMULATION

The aerodynamic forces and moments varying with δ_e and δ_a under different α and β are obtained using the CFD approach; this approach can reduce the cost of performing wind tunnel experiments and reduce design cycle time. The CFD approach was proven to be accurate in our previous study [26] considering the precision of the measurement method and the simulation errors. The pressure distribution on the MAV with no sweep simulated using the commercial software FLUENT 16.0 at $\alpha = 4^\circ$ is shown in Fig. 5; the pressure area acting on the canards is stronger than that acting on the wings. This phenomenon is in accordance with the experimental results [27], which demonstrated that the effect of downwash caused by the canards reduces the aerodynamic loads on the wings, causing the aerodynamic variation of the canards to be greater than the variation of the wings having the same sweep angle.

The basic nondimensional aerodynamic coefficients are acquired using the following equations based on the aerodynamic forces and moments obtained by the CFD approach:

$$\begin{aligned} L &= 0.5\rho V^2 S C_L, & D &= 0.5\rho V^2 S C_D, & Y &= 0.5\rho V^2 S C_Y \\ \bar{L} &= 0.5\rho V^2 S b C_l, & M &= 0.5\rho V^2 S c_A C_m, & N &= 0.5\rho V^2 S b C_n \end{aligned} \quad (4)$$

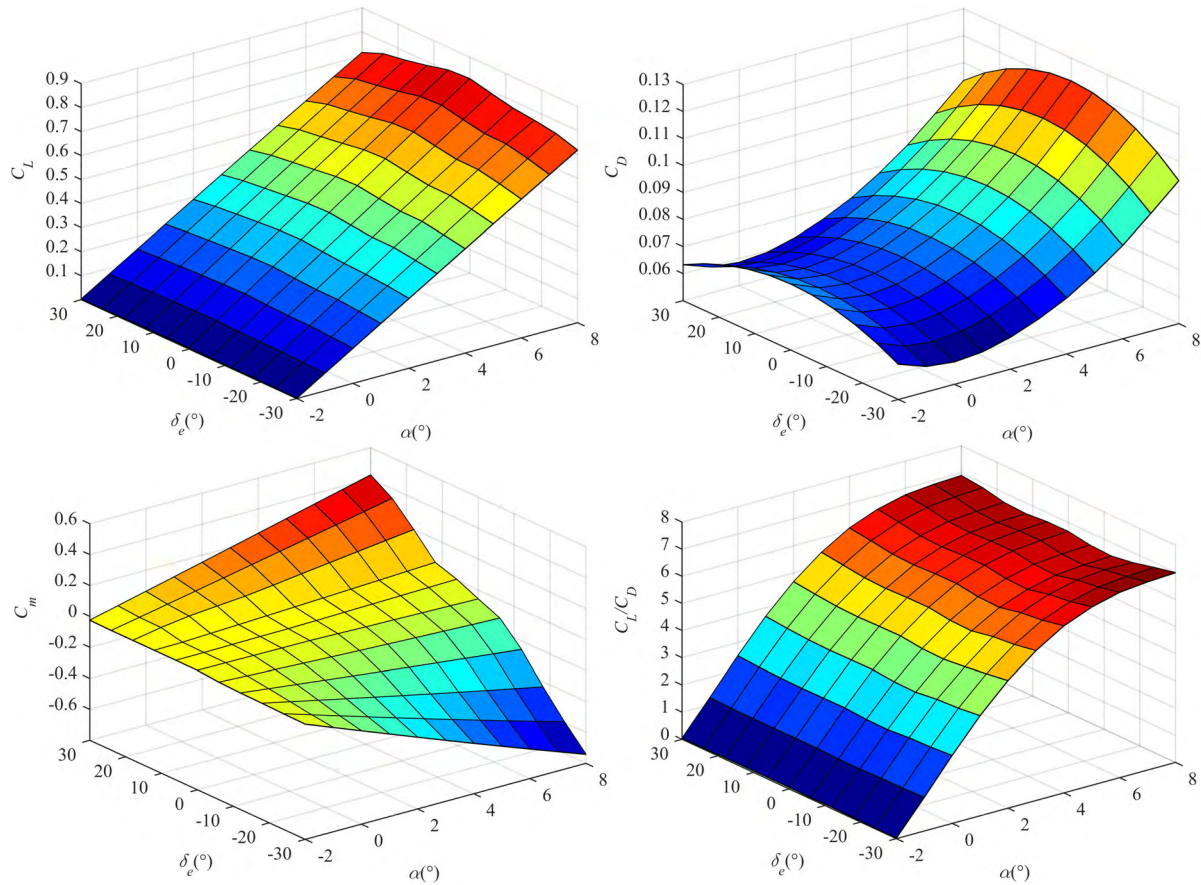


FIGURE 6. Aerodynamic coefficients under the condition of symmetric morphing ($\beta = 0^\circ$).

where L , D , Y , $x\bar{L}$, M , and xN are the lift, drag, side force, roll moment, pitch moment, and yaw moment of the MAV, respectively, ρ is the density, V is the flight velocity, S is the wing area, b is the wing span, and c_A is the mean aerodynamic chord. However, the CFD method is not suitable for calculating the aerodynamic derivatives because this approach requires many calculations and a complex analysis process. The VLM is used to estimate the aerodynamic derivatives with the same configuration; the VLM is widely used in the community and is particularly accurate for analyzing MAVs with thin wings [14], [28].

According to symmetric morphing, the aerodynamic forces and moments of the variable sweep MAV at $\beta = 0^\circ$ with different attack angles are presented in Fig. 6. Symmetric morphing primarily affects longitudinal motion; thus, for a sideslip angle of $\beta = 0^\circ$, the side force, roll moment and yaw moment are all zero and nearly invariable with symmetric morphing. The lift and drag gradually decrease as δ_e changes from 0° to 30° or -30° , whereas the lift-drag ratio increases gradually; this trend illustrates that the lift varies within a small range and the drag varies considerably with increases in the deformation amplitude. The maximum nose-up and nose-down pitch moments generated by symmetric sweep morphing are $0.618 \text{ N} \cdot \text{m}$ and $-1.21 \text{ N} \cdot \text{m}$, respectively,

at $\alpha = 4^\circ$, and increase with increases in the attack angle as well as the lift and drag.

According to asymmetric morphing on the left side, the aerodynamic forces and moments of the variable sweep MAV at $\alpha = 4^\circ$ with different sideslip angles are presented in Fig. 7. Asymmetric morphing primarily affects lateral motion but can also affect the longitudinal aerodynamic coefficients to some degree. Moreover, under the condition of symmetric morphing, an MAV experiencing more deformation will have a smaller lift and drag. Furthermore, regardless of the sign of the sideslip angle, the lift and drag decrease with increases in the sideslip angle. A negative roll moment is generated by the sweep variation of the left side of the MAV, and the maximum moment is $-0.487 \text{ N} \cdot \text{m}$ when $\beta = 0^\circ$; variations in the sideslip do not change this moment significantly. A small side force and positive yaw moment are generated with the MAV morphing at $\beta = 0^\circ$, and the magnitudes are proportional to the sideslip angle. When $\beta = 0^\circ$, the change in the pitch moment as the MAV morphs causes the MAV to nose-down, and the sideslip angle will exacerbate the extent of nosing-down. The effect causes the dynamics to experience cross-coupling, which is undesirable and is a considerable challenge for flight control.

III. FLIGHT DYNAMICS MODELING BASED ON THE KANE METHOD

An accurate and insightful dynamic model must be built as the foundation of controller design and mission simulation. In the large-scale morphing process of the variable sweep MAV, various parameters, such as the aerodynamic force and moment, moment of inertia, center of mass and aerodynamic center, have distinct changes and exhibit clear time-varying and nonlinear characteristics. As a result, standard rigid-body dynamics equations will not be applicable. To remedy this situation, Obradovic *et al* relaxed the rigidity of the morphing aircraft to make the inertia tensor an explicit function of time that depends on the displacements and rotations of the various components [16]. However, this method will generate many moment of inertia derivative arguments, making the dynamics equations more complex.

Another approach is to apply the methods of multibody dynamics, treating the entire aircraft as several separate rigid bodies; in this approach, the inertia moment and inertia tensor of each body are constant. Compared with the Lagrange method, modeling using the Kane method greatly reduces the differential operations through the introduction of vector mechanics and analytical mechanics [29]. Moreover, modeling using the Kane method benefits the linearization of the dynamics equations. Thus, the nonlinear dynamics equations of the variable sweep MAV will be formulated using the Kane method.

A. GENERALIZED COORDINATE AND GENERALIZED VELOCITY

The MAV is comprised of a fuselage and four active airfoils; the moment of inertia and product of inertia of each component do not vary over time. The center of mass of the aircraft shifts during the morphing process; thus, the origin of the body coordinate system $O_b x_b y_b z_b$ is located at the center of mass of the fuselage instead of the aircraft, and the ground coordinate system is described as $O_g x_g y_g z_g$, as shown in Fig. 3. Vertical tails have only a slight influence and are typically neglected in the modeling process.

The generalized coordinates have the minimum number of variables that could satisfy the constraints and ascertain a unique configuration in the inertial frame of reference. We chose $[x, y, z, \phi, \theta, \psi, h_1, h_2, h_3, h_4]^T$ as the generalized coordinates: $[x, y, z]^T$ is the position of O_b in the ground coordinate system; ϕ , θ and ψ are the bank angle, pitch angle and yaw angle, respectively; and h_1, h_2, h_3 and h_4 are the sweep angles that define the deformation extent of the MAV. The generalized velocity is a first-order differential equation for the generalized coordinate. The attitude angles and angular velocities are measured in the body axes; thus, for further analysis and control system design, we chose $\mathbf{x} = [u, v, w, p, q, r, \eta_1, \eta_2, \eta_3, \eta_4]^T$ as the generalized velocities. $[u, v, w]^T$ and $[p, q, r]^T$ are the flight velocity and angular velocity in the body coordinate system, respectively. η_i is the differential of h_i with respect to time, with $i = 1, 2, 3$ and 4.

The relationship between the generalized coordinates and generalized velocities can be expressed as

$$\begin{cases} [u, v, w]^T = \mathbf{S}_{bg}[\dot{x}, \dot{y}, \dot{z}]^T \\ [p, q, r]^T = \mathbf{Q}[\dot{\phi}, \dot{\theta}, \dot{\psi}]^T \\ [\eta_1, \eta_2, \eta_3, \eta_4]^T = [\dot{h}_1, \dot{h}_2, \dot{h}_3, \dot{h}_4]^T \end{cases} \quad (5)$$

where \mathbf{S}_{bg} and \mathbf{Q} are transition matrices and are expressed as:

$$\mathbf{S}_{bg} = \begin{bmatrix} c\theta c\psi & c\theta s\psi & -s\theta \\ s\theta c\psi s\phi - s\psi c\phi & s\theta s\psi s\phi + c\psi c\phi & c\theta s\phi \\ s\theta c\psi c\phi + s\psi s\phi & s\theta s\psi c\phi - c\psi s\phi & c\theta c\phi \end{bmatrix} \quad (6)$$

$$\mathbf{Q} = \begin{bmatrix} 1 & 0 & -\sin\theta \\ 0 & \cos\phi & \sin\phi \cos\theta \\ 0 & -\sin\phi & \cos\phi \cos\theta \end{bmatrix} \quad (7)$$

B. PARTIAL VELOCITY AND PARTIAL ANGULAR VELOCITY

The flight velocity and angular velocity of the MAV in the body coordinate system can be formed as

$$\begin{cases} \mathbf{v} = u\mathbf{i} + v\mathbf{j} + w\mathbf{k} \\ \boldsymbol{\omega} = p\mathbf{i} + q\mathbf{j} + r\mathbf{k} \end{cases} \quad (8)$$

Because the body coordinate system is fixed on the fuselage, the velocity and angular velocity of the fuselage can be expressed as

$$\begin{cases} \mathbf{v}_f = u\mathbf{i} + v\mathbf{j} + w\mathbf{k} \\ \boldsymbol{\omega}_f = p\mathbf{i} + q\mathbf{j} + r\mathbf{k} \end{cases} \quad (9)$$

Because all of the airfoils rotate around the body axis z , the angular velocities are

$$\boldsymbol{\omega}_i = p\mathbf{i} + q\mathbf{j} + (r + \eta_i)\mathbf{k} \quad (10)$$

where $i = 1, 2, 3$ and 4.

When there is no sweep, in body coordinate we define

$$\mathbf{r}_{O_b O_i} = x_i\mathbf{i} + y_i\mathbf{j} + z_i\mathbf{k} \quad (11)$$

$$\mathbf{r}_{O_i O'_i} = x'_i\mathbf{i} + y'_i\mathbf{j} + z'_i\mathbf{k} \quad (12)$$

where $x_1 = x_1 = a_c, x_3 = x_4 = -a_w, y_i = (-1)^i b_f, z_1 = z_2 = -z_3 = -z_4 = c, x'_i = (-1)^{1+i} \sin x h_i, y'_i = (-1)^i l \cos h_i$, and $z'_i = 0$. The velocity of the airfoils is

$$\mathbf{v}_i = \mathbf{v}_f + \boldsymbol{\omega}_f \times \mathbf{r}_{O_b O_i} + \boldsymbol{\omega}_i \times \mathbf{r}_{O_i O'_i} \quad (13)$$

where $i = 1, 2, 3$ and 4.

Transforming (10), (11) and (12) to functions of the generalized velocities as given in (13), the corresponding partial velocity and partial angular velocity can be acquired as

$$\begin{cases} \mathbf{v}_i = [\mathbf{v}_1^i, \dots, \mathbf{v}_k^i, \dots, \mathbf{v}_{10}^i] \mathbf{x} \\ \boldsymbol{\omega}_i = [\boldsymbol{\omega}_1^i, \dots, \boldsymbol{\omega}_k^i, \dots, \boldsymbol{\omega}_{10}^i] \mathbf{x} \end{cases} \quad (14)$$

where \mathbf{v}_k^i and $\boldsymbol{\omega}_k^i$ represent the k th partial angular velocity and partial velocity of component i , respectively, $i = f, 1, 2, 3$ and 4 denote the fuselage, left canard, right canard, left wing and right wing, respectively, and $k = 1, 2, \dots, 10$ denote the corresponding generalized velocities.

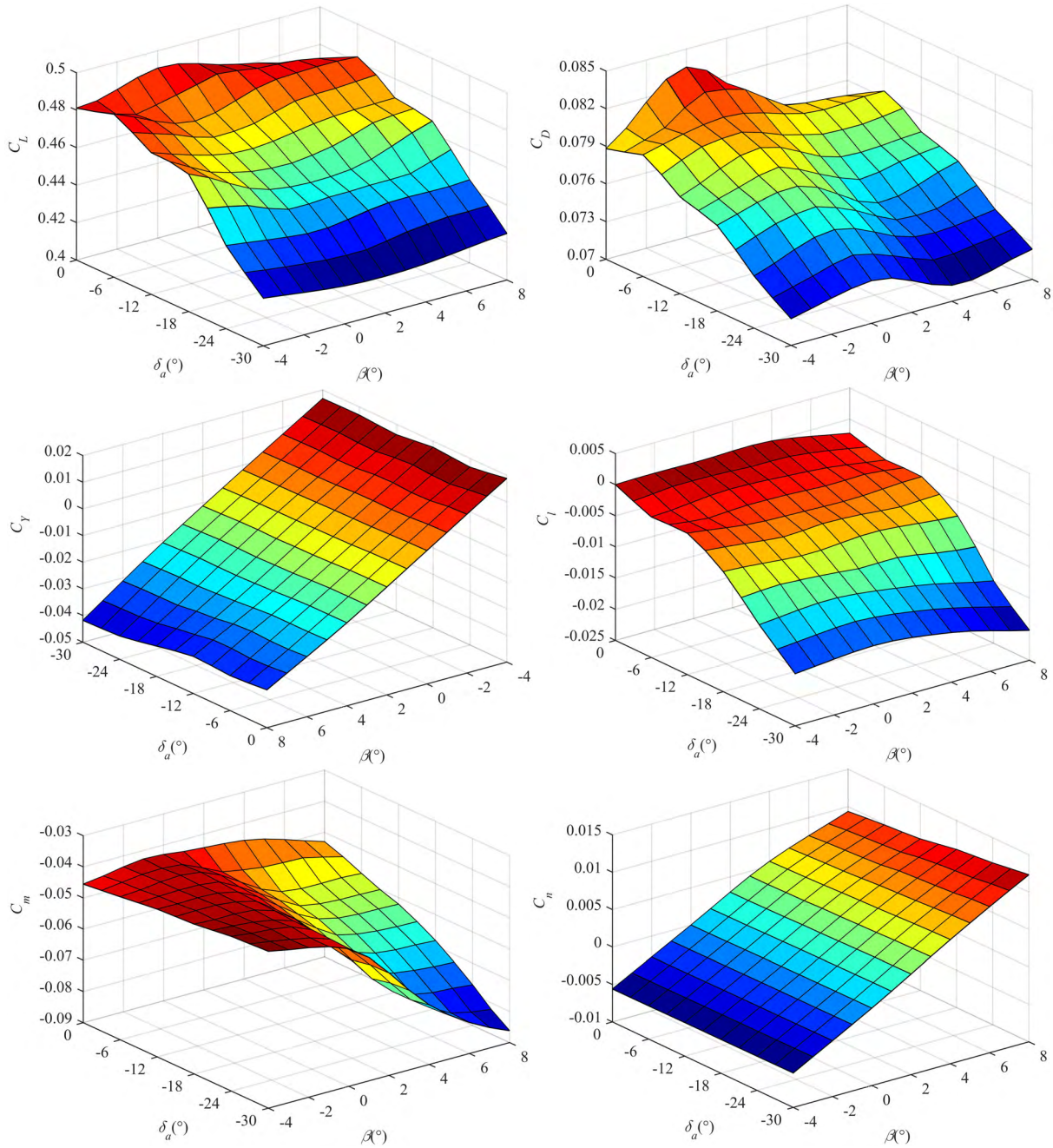


FIGURE 7. Aerodynamic coefficients under the condition of asymmetric morphing ($\alpha = 4^\circ$).

C. ACTIVE FORCE AND ACTIVE MOMENT

The active force of the fuselage is contributed by the gravity of the fuselage, the thrust and the aerodynamic force and can be expressed as

$$\mathbf{F}_f = S_{bg}[0, 0, m_f g]^T + [P, 0, 0]^T + \mathbf{S}_{ab}^T[-D_f, Y_f, -L_f]^T \quad (15)$$

where g is the acceleration of gravity, m_f is the mass of the fuselage, P is the thrust, D_f , Y_f and L_f are the drag, side force and lift on the fuselage, respectively.

The active moment of the fuselage is contributed by the reactive force of the driving torques and the side force while assuming the lift and drag act on the mass center and is expressed as

$$\mathbf{M}_f = [0, 0, T_1 + T_2 + T_3 + T_4]^T + [-0.5l_f, 0, 0]^T \times \mathbf{S}_{ab}^T[0, Y_f, 0]^T \quad (16)$$

where T_i is the driving torque of the airfoil, $i = 1, 2, 3$ and 4, and l_f is the length of the fuselage.

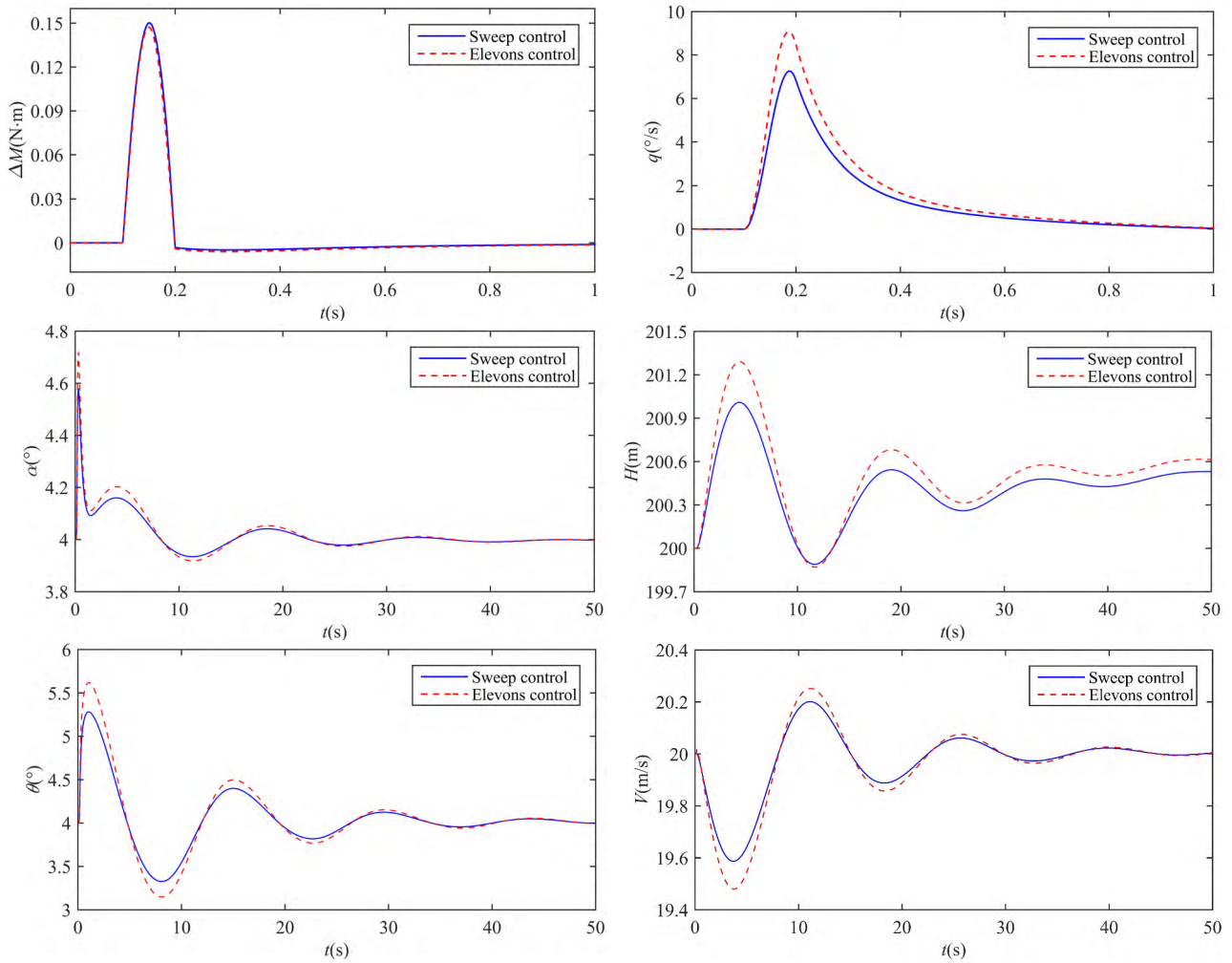


FIGURE 8. Open-loop dynamic responses caused by symmetric morphing.

The active force of the airfoil contributed by the gravity and aerodynamic force can be expressed as

$$\mathbf{F}_i = \mathbf{S}_{bg}[0, 0, m_i g]^T + \mathbf{S}_{ab}^T[-D_i, Y_i, -L_i]^T \quad (17)$$

where m_i is the mass of airfoil and is equal to m_a and $i=1, 2, 3$ and 4 .

O_{ia} is the aerodynamic center of each airfoil, and in the body coordinate is defined as

$$\mathbf{r}_{O_i O_{ia}} = x_{ia} \mathbf{i} + y_{ia} \mathbf{j} \quad (18)$$

Thus, the active moments of the airfoil are

$$\mathbf{M}_i = [0, 0, -T_i]^T + (\mathbf{r}_{O_i O_{ia}} - \mathbf{r}_{O_i O'_i}) \times \mathbf{S}_{ab}^T[-D_i, Y_i, -L_i]^T \quad (19)$$

where $i=1, 2, 3$ and 4 .

D. INERTIA FORCE AND INERTIA MOMENT

To obtain the inertia moment, the angular acceleration vector and acceleration vector must be obtained first. Taking the derivative of the angular velocity can be used to acquire the

angular acceleration; the acceleration of the mass center of each component in the body coordinate system can be written as

$$\mathbf{a}_f = \dot{\mathbf{v}}_f + \boldsymbol{\omega}_f \times \mathbf{v}_f \quad (20)$$

$$\mathbf{a}_i = \mathbf{a}_f + \dot{\boldsymbol{\omega}}_f \times \mathbf{r}_{O_b O_i} + \boldsymbol{\omega}_f \times \dot{\mathbf{r}}_{O_b O_i} + \dot{\boldsymbol{\omega}}_i \times \mathbf{r}_{O_i O'_i} + \boldsymbol{\omega}_i \times \dot{\mathbf{r}}_{O_i O'_i} \quad (21)$$

The inertia moment of component i is given by

$$\dot{\mathbf{H}}_i = \dot{\mathbf{J}}_i \boldsymbol{\omega}_i + \mathbf{J}_i \dot{\boldsymbol{\omega}}_i + \boldsymbol{\omega}_i \times \mathbf{J}_i \boldsymbol{\omega}_i \quad (22)$$

where \mathbf{H}_i is the angular momentum, \mathbf{J}_i is the inertia matrix written as (23), $i=1, 2, 3$ and 4 , and $\mathbf{J}_1 = \mathbf{J}_2 = \mathbf{J}_3 = \mathbf{J}_4 = \mathbf{J}_a$.

$$\mathbf{J}_i = \begin{bmatrix} J_x^i & -J_{xy}^i & -J_{xz}^i \\ -J_{yx}^i & J_y^i & -J_{yz}^i \\ -J_{zx}^i & -J_{zy}^i & J_z^i \end{bmatrix} \quad (23)$$

The parameters of the inertia matrix are shown in Table 1. The fuselage and airfoils are all single rigid bodies; thus, $\dot{\mathbf{J}}_i = 0$.

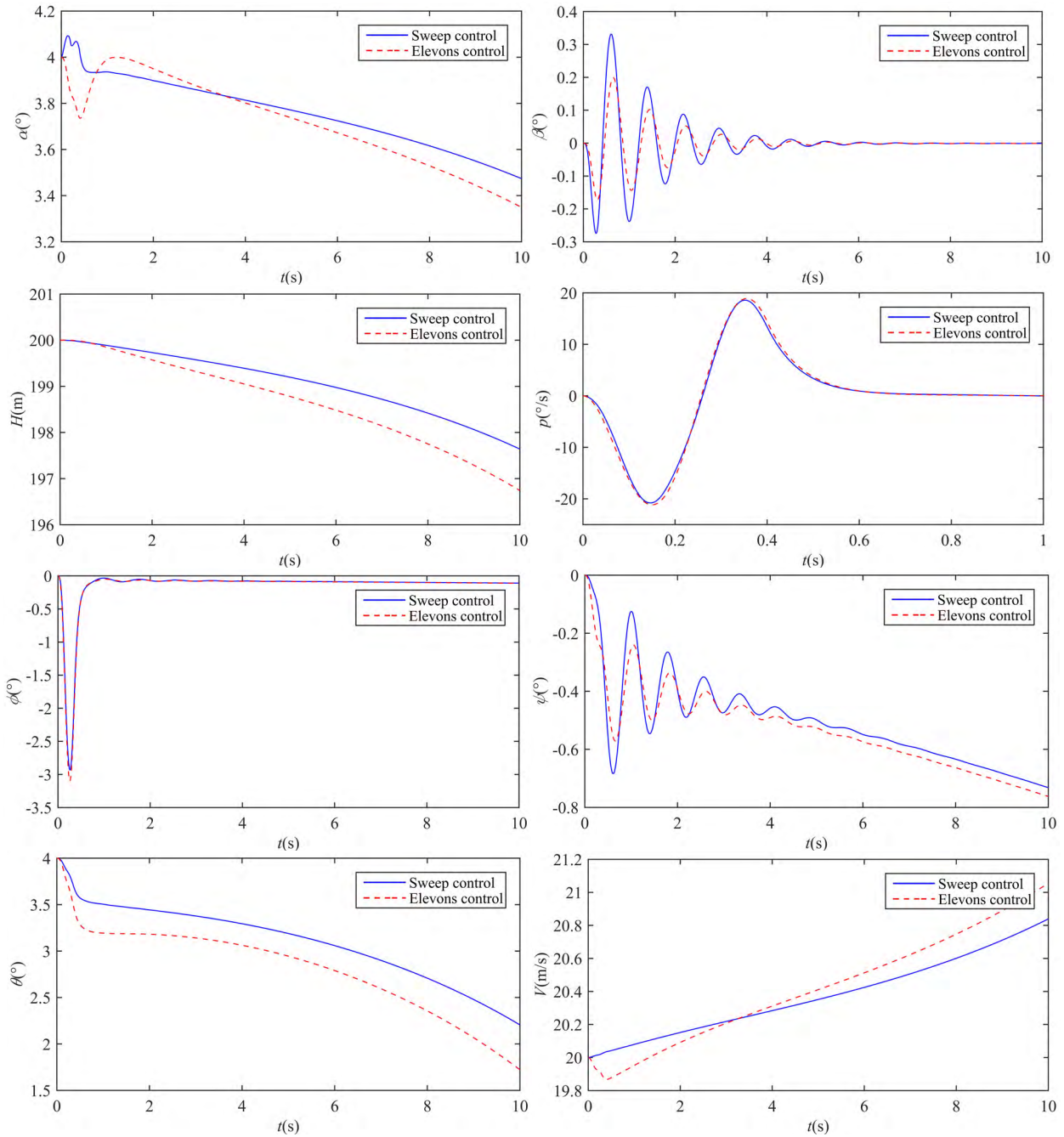


FIGURE 9. Open-loop dynamic responses caused by asymmetric morphing.

E. KANE DYNAMIC EQUATIONS

By substituting the partial velocity, partial angular velocity, active forces, active moments, inertia forces and inertia moments acquired from the previous formulas into (24), the generalized active forces \tilde{Q}_k and \tilde{Q}_k^* and the generalized inertia forces can be obtained as

$$\begin{cases} \tilde{Q}_k = \sum_i (F_i \cdot v_k^i + M_i \cdot \omega_k^i) \\ \tilde{Q}_k^* = \sum_i [(-m_i a_i) \cdot v_k^i - \dot{H}_i \cdot \omega_k^i] \end{cases} \quad (24)$$

where $i = 1, 2, 3$ and 4. The basic Kane equations are written as

$$\tilde{Q}_k + \tilde{Q}_k^* = 0 (k = 1, 2, \dots, 10) \quad (25)$$

The Kane equations represent the six-degree-of-freedom nonlinear time-varying dynamic model and the four actuators' dynamics. The detailed expressions of the nonlinear dynamic model are shown in Appendix. The equations for the four actuators' dynamics are highly complex, and the response time of the actuators is short; thus, we assumed that

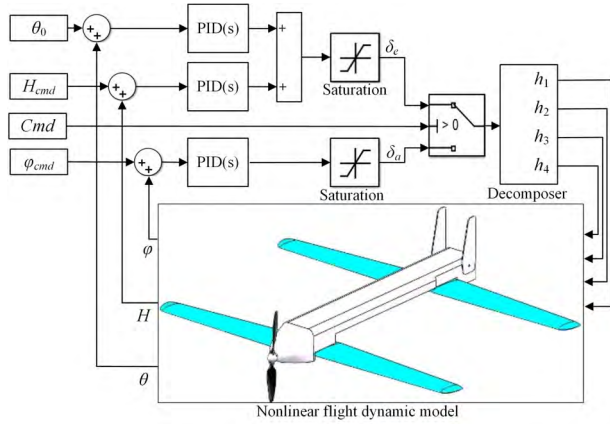


FIGURE 10. Closed-loop control structure based on sweep control.

the actuators can provide the required moments and power to assert the appropriate behavior, and a suitable second-order system is used to formulate the transient response of the actuators as:

$$\ddot{\eta}_i = \omega_n^2(h_{ci} - h_i) - 2\zeta_n\omega_n\dot{\eta}_i \quad (26)$$

where $i = 1, 2, 3$ and 4 , ω_n is the natural frequency, ζ_n is the damping ratio, and h_{ci} is the desired control input. This approach ignores the effect of aerodynamic load on the actuator dynamics, and ω_n is limited by the performance of the actuators [18].

By combining (A1)-(A6) and (26), the nonlinear dynamics model can be described by

$$\dot{\mathbf{x}} = \mathbf{A}(\mathbf{u})\mathbf{x} + \mathbf{B}(\mathbf{u}) \quad (27)$$

where \mathbf{x} is the state variable, $\mathbf{u} = [\delta_e, \delta_a, \delta_T]^T$ is the control input, δ_e and δ_a refer to (1) and (2), respectively, and δ_T is the thrust control. \mathbf{A} and \mathbf{B} are the configuration matrices that vary with \mathbf{u} , and they will determine the dynamic responses of the morphing MAV. The control input in the traditional control mode can typically affect only the control moment, and the effect on the configuration matrix is ignored. This aspect is the difference between the sweep control mode and traditional control mode.

IV. DYNAMIC CHARACTERISTICS ANALYSES AND FLIGHT CONTROL

In this section, open-loop dynamic simulation is performed based on the nonlinear dynamic model to compare the control effectiveness between variable sweep control and elevons control. Then, the closed-loop flight simulation is presented to verify the feasibility and effects of variable sweep for flight control.

A. OPEN-LOOP DYNAMIC RESPONSES COMPARED WITH ELEVONS CONTROL MODE

Morphing is typically used to enhance the aerodynamic performance in variable environments because the large inertia and limited material strength lead to a slow dynamic response

of morphing. However, the small size and light airfoils in the MAV configuration enable the use of sweep morphing as the only control input. Under the condition of no rudder, the sweep control is equivalent to the elevons control, but the control processes are different. The open-loop dynamic responses of sweep control based on the nonlinear dynamic model compared with these achieved through elevons control are shown in Figs. 8 and 9. The initial condition is straight and level flight at $H = 200$ m, $V = 20$ m/s, and $\alpha = 4^\circ$ in the static standard atmosphere.

The simulation results shown in Fig. 8 are the dynamic responses at the maximum symmetric morphing magnitude $|\delta_e| = 12^\circ$, which is less than the achievable maximum sweep angle, and the compared results were obtained with no morphing configuration at the same magnitude pitch moment response using elevons control. The responsive pitch moment ΔM causes α , θ and pitch angular velocity q to all increase in the preliminary stage that is characteristic of a typical short period. In addition, the variations are slightly stronger when using the elevons control mode because as the sweep varies, the mass center of the wings shift forward to generate a slight nose-down pitch moment about the gravity center of the MAV. After the input response finishes, the morphing MAV returns to the configuration of no sweep, α and q recover rapidly to the initial values; therefore, the short-period mode is stable. Because the sweep morphing process is brief, the phugoid motion parameters, height H and velocity V both change slightly and then exhibit a gradual convergence to the equilibrium state, and θ mainly shows the phugoid characteristics and is convergent, so the phugoid mode is also stable. Meanwhile, H exhibits a slight increment after suffering the effect of input response. Moreover, because of the forward shift in the center of mass, the increment in H generated by the sweep control is smaller than that by the elevons control once the process is complete, but the difference is less than 0.1 m. There is no lateral dynamic response during symmetric morphing.

Fig. 9 shows the dynamic responses at the maximum asymmetric morphing magnitude of $|\delta_a| = 15^\circ$, which is less than the maximum sweep angle that can be achieved. The compared results were obtained with no morphing configuration at the same magnitude roll moment response using elevons control. Asymmetric morphing drives longitudinal and lateral dynamic responses simultaneously. Asymmetric morphing induces not only a roll moment but also a coupled nose-down pitch moment, affected by the pitch angle; H and θ suffer a sustained decline with decreases in α and increases in V . When the MAV banks left, the MAV generates a left sideslip angle and yaws to the left, and the variation of β gradually slows down as the bank angle ϕ decreases. Furthermore, under symmetric morphing, the dynamic responses caused by elevons control are slightly stronger than those caused by sweep control because the shift in the center of mass is contrary to rolling during asymmetric morphing. In other words, the coupled longitudinal motion is weaker while using asymmetric morphing for lateral attitude control, as expected.

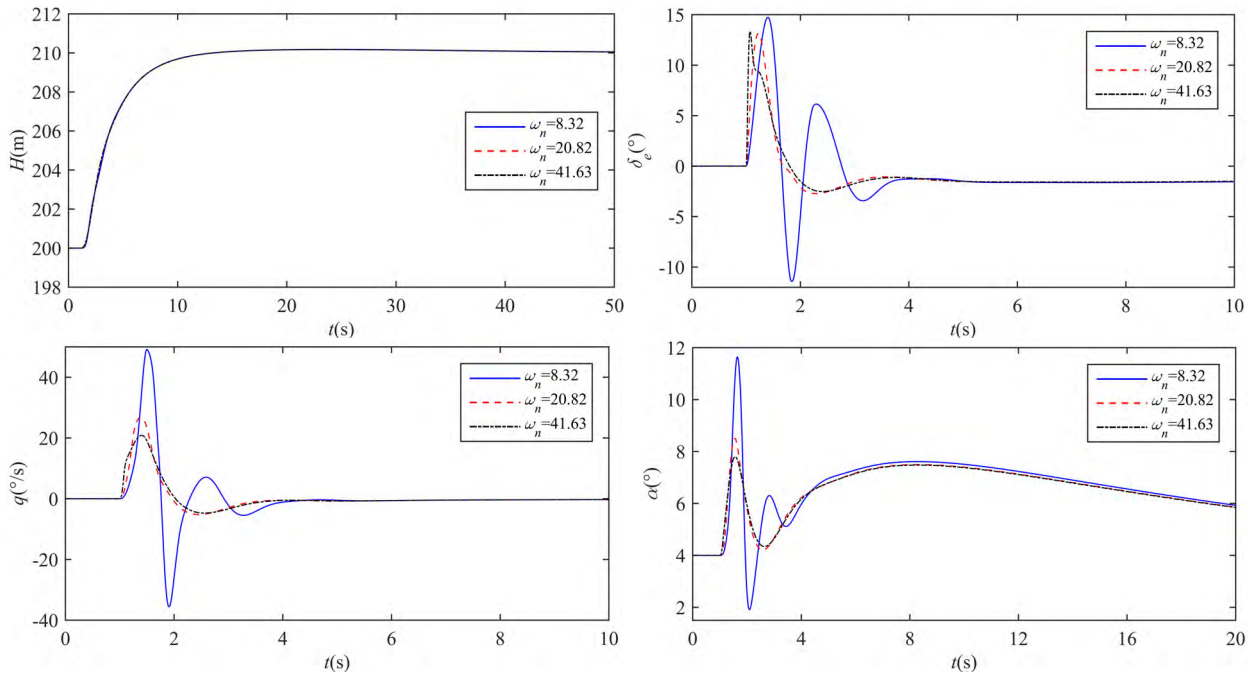


FIGURE 11. Height tracking responses with a 10 m ascending command with different ω_n .

It is observed that the dynamic responses of the two control mode are almost coincident both in the longitudinal and lateral direction, and the effectiveness of the variable sweep control mode is a slightly weaker than that of the elevens control mode. The differences are mainly due to the shift in mass center during sweep morphing, which will generate a moment opposite moment to the main control moment. However, the positive influence is a weaker coupling between the longitudinal motion and lateral motion.

B. FLIGHT CONTROL DESIGN AND CLOSED-LOOP FLIGHT SIMULATION

In general, practical MAV systems are essentially nonlinear and unknown nonlinearities exist because the practical systems are hardly described precisely by the mathematical models. The adaptive control approach is an effective control method for nonlinear systems to address unknown nonlinearities, and combining the backstepping technique with adaptive fuzzy control or adaptive neural control is extensively applied to various classes of nonlinear systems, such as interconnected nonlinear systems [30], nonlower triangular nonlinear systems [31], multiinput multioutput time-delay nonlinear systems [32] and high-order nonlinear systems [33]. The adaptive control approach has the advantage under unknown nonlinearities, but it is very complex and is considered outside the scope of the current paper. In this paper, the flight control system is built using a cascaded proportional-integral-derivative (PID) controller which is also widely and successfully used in nonlinear systems with various uncertainties.

The symmetric morphing magnitude δ_e and asymmetric morphing magnitude δ_a are innovative control inputs that

serve in the roles of conventional elevators and ailerons for flight control. The closed-loop control structure for the variable sweep MAV is shown in Fig. 10. The height controller, which is integrated with the inner loop controller for pitch stabilization and control, is considered to be the longitudinal autopilot, and the heading controller is considered to be the lateral autopilot, which comprises an inner loop controller for roll and sideslip stabilization and control. The two control channels work in order. When the command calls for longitudinal motion, the height controller switches on, whereas when the command calls for lateral motion, the heading controller switches on. Then, the decomposer decomposes the output δ_e or δ_a signal into the four corresponding sweep angle signals.

The detailed descriptions of the height and heading controller based on the classical PID control approach are expressed by (27) and (29).

Height controller

$$\begin{cases} \Delta\delta_e = K_{\theta p}\Delta\theta + K_{\theta i}\int\theta dt + K_{\theta d}q + K_{H_p}\Delta H \\ \quad + K_{H_i}\int H dt + K_{H_d}\dot{H} \\ \Delta\theta = \theta_0 - \theta \\ \Delta H = H_{cmd} - H \end{cases} \quad (28)$$

Heading controller

$$\begin{cases} \Delta\delta_a = K_{\varphi p}\Delta\varphi + K_{\varphi i}\int\varphi dt + K_{\varphi d}r \\ \Delta\varphi = \varphi_{cmd} - \varphi \end{cases} \quad (29)$$

where K_{*p} , K_{*i} and K_{*d} represent the proportional, integral and differential gain, respectively, and “*” represents θ ,

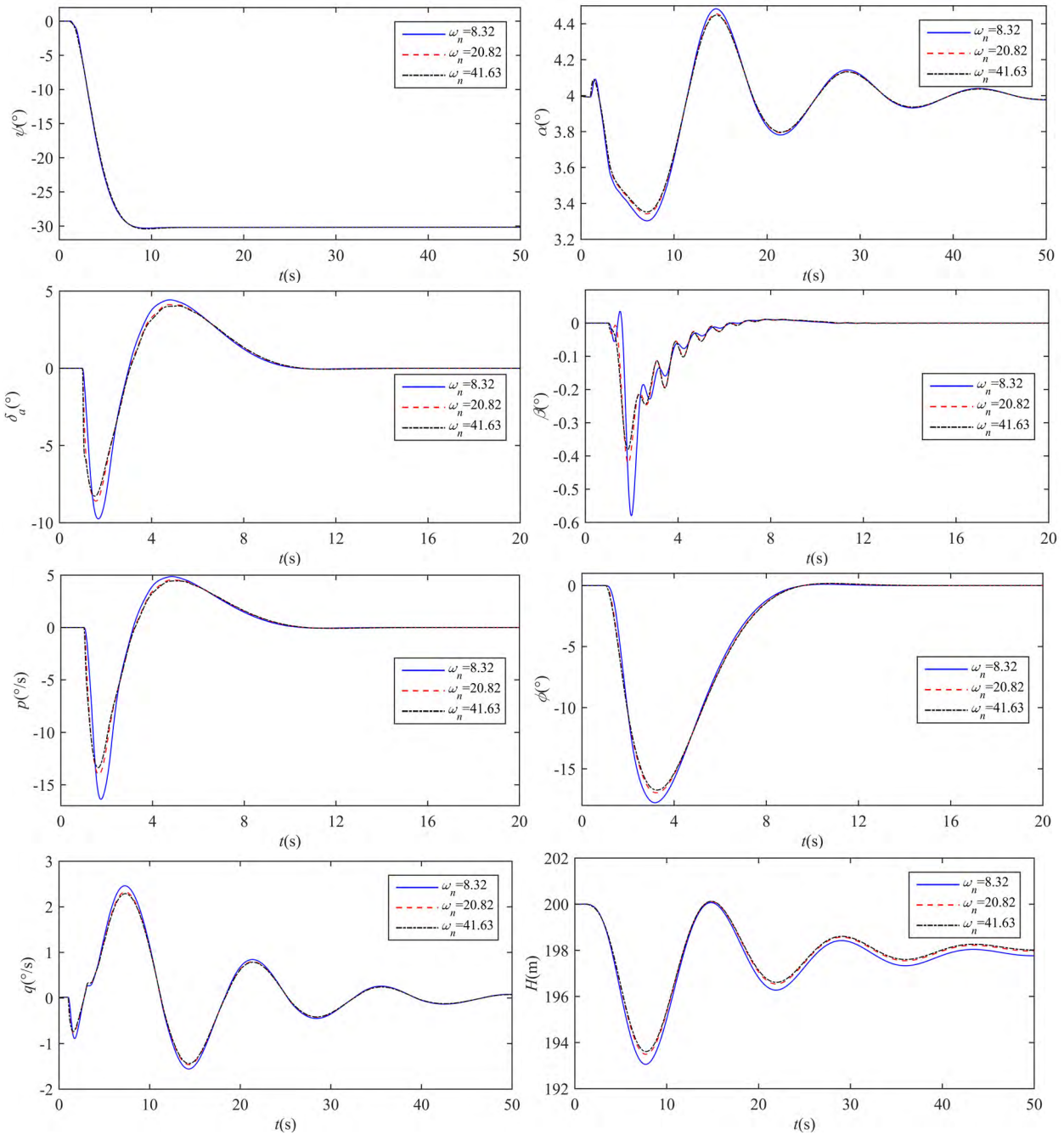


FIGURE 12. Yaw tracking responses with a 30° turning left command with different ω_n .

H and φ . θ_0 represents the initial theta angle, H_{cmd} and φ_{cmd} are the input commands.

To validate the control performance of the sweep control mode, height and yaw angle tracking were simulated based on the nonlinear dynamic model. Moreover, the influences of the actuator response rate were analyzed for $\omega_n = 8.32$, 20.82 and 41.63 rad/s; the corresponding rise times are 0.5 s, 0.2 s and 0.1 s, respectively, and $\zeta_n = 0.7$. The actuator has a faster dynamic response when ω_n is larger. The initial condition is straight and level flight at $H = 200$ m,

$V = 20$ m/s, and $\alpha = 4^\circ$. The throttle δ_T response is not considered temporarily and remains constant.

The height tracking responses for a 10 m ascending command are shown in Fig. 11. The simulation results indicate that the height responses can all track the desired height well in the three cases, without any sweep saturation, and the rising progresses for approximately 10 s. Moreover, the variation trends of α and q are very similar to the change in δ_e , and the longitudinal state variables tend to be stable after the MAV reaches the targeted height, which demonstrates

that the height controller responds quickly with high control precision and can maintain stable longitudinal motion. One shortcoming is that the height rising efficiency is not high, and the change in α is exceeds 3.5° . However, an overly large attack angle may cause stalling and needs to be coordinated with the throttle output to achieve better performance.

From the height tracking responses for different actuator response rates, it is observed that the amplitudes of the responses of δ_e , q and α are larger and the oscillation time is longer when ω_n is smaller. In other words, if the actuator response rate is slower, the time of that MAV is in an unstable state will be greater, and therefore, a longer oscillation time is needed to reach the steady state. This situation is obvious, especially when $\omega_n = 8.32$ rad/s, and δ_e experiences a significant negative value compared with those for the other two cases shown in Fig. 11.

The yaw tracking responses with a 30° turning left command are shown in Fig. 12. The simulation results indicate that the yaw responses can track to the desired yaw angle within 7 s in the three cases, without any sweep saturation; furthermore, the sideslip angle of the responses can be eliminated by asymmetric morphing, and the other lateral motion parameters and the coupled longitudinal motion parameters all converge gradually to the equilibrium state. The simulation results illustrate that the heading controller can also work well with high control precision and can keep the MAV stable. However, the yaw control by asymmetric morphing is found to produce a slight height decrease of less than 2 m, so the heading controller must cooperate with the height controller to maintain altitude after the yaw control.

The influence of ω_n is similar to the height tracking responses, and a smaller ω_n results in stronger amplitude responses for all the motion parameters. Nevertheless, the influence is not as obvious as the situation with the height tracking responses, except for β .

V. CONCLUSION

In this paper, symmetric and asymmetric sweep morphing modes were proposed as new control inputs to replace the conventional control surfaces for flight control; the innovative concept was applied in a novel tandem-wing MAV that can be folded into and launched from a tubular catapult. The four sweep angles of the MAV were planned as symmetric and asymmetric morphing to maximally eliminate the reactive force between airfoils and fuselage during morphing. The effects of sweep morphing on the aerodynamic characteristics were investigated using CFD and VLM based on the quasi-steady assumption; the symmetric and asymmetric sweep morphing modes generated considerable pitch and roll moments, respectively. An accurate nonlinear multibody dynamic model of the variable sweep MAV was built using the Kane method. Based on the nonlinear dynamic model, the open-loop dynamic responses of sweep morphing were analyzed and compared with the responses caused by the elevons control mode. A flight control law was also designed using the classical PID control approach and was

demonstrated with a closed-loop simulation of height and yaw tracking. The nonlinear simulation results demonstrated the following:

(1) The sweep control mode produces weaker coupling between the longitudinal and lateral dynamics than the elevons control mode with the same magnitude of control moment.

(2) The use of variable sweep for flight control was verified to be feasible and effective; although yaw control will provide only a slight change in height, it can be adjusted by the height controller after the yaw control.

(3) The slower actuator response rate will cause stronger amplitude responses and a longer oscillation time for the motion parameters.

APPENDIX

The detailed six-degrees of freedom nonlinear dynamic model is expressed by the following:

$$F_x = m(\dot{u} + wq - vr) - \sum_{i=1}^4 m_a[y'_i(\dot{r} + \dot{\eta}_i) + \dot{y}'_i(r + \eta_i)] \quad (A1)$$

$$F_y = m(\dot{v} + ur - wp) + \sum_{j=1}^4 m_a[(x_i + x'_i)\dot{r} + x'_i\dot{\eta}_j + \dot{x}'_i(r + \eta_i)] \quad (A2)$$

$$F_z = m(\dot{w} + vp - uq) + \sum_{j=1}^4 m_a[y'_i\dot{p} - (x_i + x'_i)\dot{q} + \dot{y}'_ip - \dot{x}'_iq] \quad (A3)$$

$$\begin{aligned} \bar{L} = & -m_ag \cos \theta \cos \phi \sum_{i=1}^4 y'_i \\ & + J_x^f \dot{p} + qr(J_z^f - J_y^f) - J_{xz}^f(\dot{r} + pq) + 4J_x^a \dot{p} \\ & + 4qr(J_z^a - J_y^a)\{-z_i[\dot{v} + ur - wp + (x_i + x'_i)\dot{r} + x'_i\dot{\eta}_i \\ & + \dot{x}'_i(r + \eta_i) - z_i\dot{p}] + m_a \sum_{i=1}^4 [\dot{w} + vp - uq + (y_i + y'_i)\dot{p} \\ & - (x_i + x'_i)\dot{q} + \dot{y}'_ip - \dot{x}'_iq](y_i + y'_i)\} \end{aligned} \quad (A4)$$

$$\begin{aligned} M = & m_ag \cos \theta \cos \phi \sum_{i=1}^4 (x_i + x'_i) \\ & + J_y^f \dot{q} + pr(J_x^f - J_z^f) + J_{xz}^f(p^2 - r^2) + 4J_y^a \dot{q} \\ & + 4(J_x^a - J_z^a)pr \\ & \times \{z_i[-y'_i\dot{r} - y'_i\dot{\eta}_i - \dot{y}'_i(r + \eta_i) + z_i\dot{q}] \\ & + m_a \sum_{i=1}^4 [-\dot{w} + vp - uq + (y_i + y'_i)\dot{p} \\ & - (x_i + x'_i)\dot{q} + \dot{y}'_ip - \dot{x}'_iq](x_i + x'_i)\} \end{aligned} \quad (A5)$$

$$\begin{aligned} N = & -m_ag \sum_{i=1}^4 [\sin \theta (y_i + y'_i) + \cos \theta \sin \phi (x_i + x'_i)] \\ & + J_z^f \dot{r} + pq(J_y^f - J_x^f) - J_{xz}^f(\dot{p} - qr) + 4J_z^a \dot{r} \end{aligned}$$

$$\begin{aligned}
& + 4pq(J_y^i - J_x^i) \\
& + m_a \sum_{j=1}^4 \{ [\dot{v} + ur - wp + (x_i + x'_i)\dot{r} + x'_i(r + \eta_i) \\
& - z_j\dot{p}](x_i + x'_i) - [\dot{u} + wq - vr - (y_i + y'_i)\dot{r} \\
& - y'_i(r + \eta_i) + z_j\dot{q}](y_i + y'_i) \} \quad (A6)
\end{aligned}$$

According to the relationship between body coordinate frame and wind coordinate the forces on the MAV are expressed as

$$\begin{cases} F_x = P - mg \sin \theta - D \cos \alpha \cos \beta - Y \cos \alpha \sin \beta \\ \quad + L \sin \alpha \\ F_y = mg \cos \theta \sin \phi - D \sin \beta + Y \cos \beta \\ F_z = mg \cos \theta \cos \phi - D \sin \alpha \cos \beta - Y \sin \alpha \sin \beta \\ \quad - L \cos \alpha \end{cases} \quad (A7)$$

where m is the mass of the MAV.

REFERENCES

- [1] P. Hardin and R. Jensen, "Small-scale unmanned aerial vehicles in environmental remote sensing: Challenges and opportunities," *GI Sci. Remote Sens.*, vol. 48, no. 1, pp. 99–111, 2011.
- [2] S. Barbarin, O. Bilgen, R. M. Ajaj, M. I. Friswell, and D. J. Inman, "A review of morphing aircraft," *J. Intell. Mater. Syst., Struct.*, vol. 22, no. 9, pp. 823–877, 2011.
- [3] E. Selitrennik, M. Karpel, and Y. Levy, "Computational aeroelastic simulation of rapidly morphing air vehicles," *J. Aircr.*, vol. 49, no. 6, pp. 1675–1686, 2010.
- [4] L. Dufour, K. Owen, S. Mintchev, and D. Floreano, "A drone with insect-inspired folding wings," in *Proc. IEEE/RSJ Int. Conf. Intell. Robots Syst.*, New York, NY, USA, Oct. 2016, pp. 1576–1581.
- [5] J. Jacob and S. Smith, "Design limitations of deployable wings for small low altitude UAVs," in *Proc. AIAA Aerosp. Sci. Meeting Including New Horizons Forum Aerosp. Expo.*, Orlando, FL, USA, Jan. 2009, p. 745.
- [6] R. Siddall, A. O. Ancel, and M. Kovač, "Wind and water tunnel testing of a morphing aquatic micro air vehicle," *Interface Focus*, vol. 7, no. 1, pp. 1–15, 2017.
- [7] L. Ben and J. Jacob, "In-flight deployment dynamics of inflatable wings," in *Proc. AIAA Aerosp. Sci. Meeting Including New Horizons Forum Aerosp. Expos.*, Orlando, FL, USA, Jan. 2010, p. 54.
- [8] B. Johnson, D. Claxton, B. Stanford, V. Jagdale, and P. Ifju, "Development of a composite bendable-wing micro air vehicle," in *Proc. AIAA Aerosp. Sci. Meeting Exhibit*, Reno, NV, USA, Jan. 2007, p. 1044.
- [9] J. Henry, D. Schwartz, M. Soukup, and A. Altman, "Design, construction, and testing of a folding-wing, tube-launched micro air vehicle," in *Proc. AIAA Aerosp. Sci. Meeting Exhibit*, Reno, NV, USA, Jan. 2005, p. 1451.
- [10] J. Ott and D. Biezad, "Design of a tube-launched UAV," in *Proc. AIAA 3rd Unmanned Unlimited Techn. Conf., Workshop Exhibit*, Chicago, IL, USA, Sep. 2004, p. 6493.
- [11] G. Q. Zhang and S. C. M. Yu, "Unsteady aerodynamics of a morphing tandem-wing unmanned aerial vehicle," *J. Aircr.*, vol. 49, no. 5, pp. 1315–1323, 2012.
- [12] L. Gao, J. Zhao, Y. Zhu, H. Jin, H. Wang, and H. Cai, "Application of cycle variable pitch propeller to morphing unmanned aerial vehicles," in *Proc. IEEE Int. Conf. Inf. Automat.*, Lijiang, China, Aug. 2015, pp. 2493–2498.
- [13] Z. Zhen, J. Jiang, X. Wang, and D. Wang, "Information fusion-based optimal attitude control for an alterable thrust direction unmanned aerial vehicle," *Int. J. Adv. Robot. Syst.*, vol. 10, no. 1, p. 43, 2013.
- [14] T. Guo, Z. Hou, and B. Zhu, "Dynamic modeling and active morphing trajectory-attitude separation control approach for gull-wing aircraft," *IEEE Access*, vol. 5, pp. 17006–17019, 2017.
- [15] M. Abdulrahim and R. Lind, "Flight testing and response characteristics of a variable gull-wing morphing aircraft," in *Proc. AIAA Guid., Navigat., Control Conf. Exhibit*, Providence, RI, USA, Aug. 2004, p. 5113.
- [16] B. Obradovic and K. Subbarao, "Modeling of flight dynamics of morphing wing aircraft," *J. Aircr.*, vol. 48, no. 2, pp. 391–402, 2011.
- [17] T. Yue, X. Zhang, L. Wang, and J. Ai, "Flight dynamic modeling and control for a telescopic wing morphing aircraft via asymmetric wing morphing," *Aerosp. Sci. Technol.*, vol. 70, pp. 328–338, Nov. 2017.
- [18] G. T. Yang, S. J. Tang, and J. Guo, "Aerodynamic optimization of a morphing UAV with variable sweep and variable span," in *Proc. Int. Conf. Comput. Sci. Syst. Eng.*, 2015, pp. 583–591.
- [19] B. T. Anderson, R. R. Meyer, and H. R. Chiles, "Techniques used in the F-14 variable-sweep transition flight experiment," *J. Aircr.*, vol. 28, no. 10, pp. 622–629, 2015.
- [20] Z. R. Manchester, J. I. Lipton, R. J. Wood, and S. Kuindersma, "A variable forward-sweep wing design for enhanced perching in micro aerial vehicles," in *Proc. AIAA Aerosp. Sci. Meeting*, Grapevine, TX, USA, Jan. 2017, p. 0011.
- [21] C. Greatwood, A. Waldoock, and T. Richardson, "Perched landings manoeuvres with a variable sweep wing UAV," *Aerosp. Sci. Technol.*, vol. 71, pp. 510–520, Dec. 2017.
- [22] J. Hall, K. Mohseni, and D. Lawrence, "Investigation of variable wing-sweep for applications in micro air vehicles," in *Proc. AIAA Infotech Aerosp.*, Arlington, VA, USA, Sep. 2005, p. 7171.
- [23] D. Grant and R. Lind, "Effects of time-varying inertias on flight dynamics of an asymmetric variable-sweep morphing aircraft," in *Proc. AIAA Atmos. Flight Mech. Conf. Exhibit*, Hilton Head, SC, USA, Aug. 2007, p. 6487.
- [24] K. Wright, "Investigating the use of wing sweep for pitch control of a small unmanned air vehicle," Ph.D. dissertation, Dept. Eng. Sci. (Aerosp. Eng.), Univ. California, San Diego, CA, USA, 2011.
- [25] L. Tong and H. Ji, "Multi-body dynamic modelling and flight control for an asymmetric variable sweep morphing UAV," *Aeronaut. J.*, vol. 118, no. 1204, pp. 683–706, 2014.
- [26] L. Gao, C. Li, H. Jin, H. Zhu, J. Zhao, and H. Cai, "Aerodynamic characteristics of a novel catapult launched morphing tandem-wing unmanned aerial vehicle," *Adv. Mech. Eng.*, vol. 9, no. 2, pp. 1–15, 2017.
- [27] F. A. Khan and T. J. Mueller, "Tip vortex/airfoil interaction for a low Reynolds number canard/wing configuration," *J. Aircr.*, vol. 28, no. 3, pp. 181–186, 1991.
- [28] A. Chakravarthy, D. Grant, and R. Lind, "Time-varying dynamics of a micro air vehicle with variable-sweep morphing," *J. Guid. Control Dyn.*, vol. 35, no. 3, pp. 890–903, 2012.
- [29] X. Zhang, Y. Huang, X. Chen, and W. Han, "Modeling of a space flexible probe-cone docking system based on the Kane method," *Chin. J. Aeronaut.*, vol. 27, no. 2, pp. 248–258, 2014.
- [30] H. Wang, W. Liu, J. Qiu, and X. Liu, "Adaptive fuzzy decentralized control for a class of strong interconnected nonlinear systems with unmodeled dynamics," *IEEE Trans. Fuzzy Syst.*, vol. 26, no. 2, pp. 836–846, Apr. 2018.
- [31] X. D. Zhao, P. Shi, X. L. Zheng, and J. H. Zhang, "Intelligent tracking control for a class of uncertain high-order nonlinear systems," *IEEE Trans. Neural Netw. Learn. Syst.*, vol. 27, no. 9, pp. 1976–1982, Sep. 2016.
- [32] X. Zhao, H. Yang, W. Xia, and X. Wang, "Adaptive fuzzy hierarchical sliding-mode control for a class of MIMO nonlinear time-delay systems with input saturation," *IEEE Trans. Fuzzy Syst.*, vol. 25, no. 5, pp. 1062–1077, Oct. 2016.
- [33] H. Wang, X. Liu, S. Li, and W. Ding, "Adaptive neural output-feedback control for a class of nonlinear triangular nonlinear systems with unmodeled dynamics," *IEEE Trans. Neural Netw. Learn. Syst.*, vol. 29, no. 8, pp. 3658–3668, Aug. 2018.



LIANG GAO received the B.S. and M.S. degrees from the Harbin Institute of Technology, Harbin, China, in 2011 and 2013, respectively, where he is currently pursuing the Ph.D. degree with the State Key Laboratory of Robotics and System. His research interests include flight dynamics and flying robot.



HONGZHE JIN received the B.S. degree in instrument science and technology from the Harbin Institute of Technology (HIT), Harbin, China, in 1999, and the Ph.D. degree in electronic engineering from Pusan National University, Busan, South Korea, in 2009. He is currently an Associate Professor with the School of Mechatronics Engineering, HIT. His research interests include modeling, analysis, control, and identification of complex systems.



HEGAO CAI is currently a Professor and a Ph.D. Candidate Supervisor with the State Key Laboratory of Robotics and System, School of Mechatronics Engineering, Harbin Institute of Technology, China.



JIE ZHAO received the B.S. and Ph.D. degrees in mechatronics engineering from the Harbin Institute of Technology (HIT), Harbin, China, in 1990 and 1996, respectively. He is currently a Professor with the School of Mechatronics Engineering, HIT. He is also the Head of the Robotics Institute and the School of Mechatronics Engineering, HIT. His research interests include industrial robots and bionic robots.



YANHE ZHU received the B.S. and Ph.D. degrees in mechatronics engineering from the Harbin Institute of Technology (HIT), Harbin, China, in 1998 and 2004, respectively. He is currently a Professor with the School of Mechatronics Engineering, HIT. His research interests include biped robots and robotic exoskeleton.

...